



Hydrogen absorption kinetics and microstructural features of TiFe_{0.8}Mn_{0.2} alloy

Ryun-Ho Kwak ^{a,b}, Taeyang Kwak ^c, Da Hye Lee ^{a,b}, Sojin Jung ^{a,b}, Jang-Won Kang ^a, Seongtak Kim ^a, Tae-Wook Na ^a, Seok Su Sohn ^{b,**}, Hyung-Ki Park ^{a,***}, Taejun Ha ^{a,*}

^a Functional Materials and Components Group, Gangwon Technology Application Division (Functional Materials), Korea Institute of Industrial Technology, Gangwon, 25440, Republic of Korea

^b Department of Materials Science and Engineering, Korea University, Seoul, 02841, Republic of Korea

^c RUAN Co., Ltd., Unit 203, 64, Gilju-ro, Bucheon-si, Gyeonggi-do, 14544, Republic of Korea

ARTICLE INFO

Handling Editor: L Murr

Keywords:

Hydrogen storage
Titanium alloy
Activated hydrogenation kinetics
SEM-EBSD
Grain size
Grain boundary length

ABSTRACT

This study investigated the microstructural features and the hydrogen absorption properties of as-cast, 10 h annealed, and 20 h annealed TiFe_{0.8}Mn_{0.2} alloy samples. TiFe with the Body-Centred Cubic (BCC) B2 structure and Fe₂Ti with the C14 Laves hexagonal structure were observed in the alloy samples, and the amount of precipitated second phase Fe₂Ti within the TiFe matrix phase was significantly reduced in both 10 h and 20 h annealed samples. During the annealing treatment, TiFe_{0.8}Mn_{0.2} alloy changes in terms of the equilibrium phase fraction and chemical composition were predicted through Thermo-Calc software calculation. When the samples were hydrogenated under 40 bar of hydrogen at 20 °C, the 20 h annealed sample absorbed 1.6 wt% H₂ within the longest time among the three samples. The maximum hydrogen absorption capacities of the three samples were found to be the same, exhibiting a value of 1.81 wt% H₂. Furthermore, the Scanning Electron Microscope – Electron Backscatter Diffraction (SEM-EBSD) results showed that the annealing treatment increased the grain size of the B2 matrix by decreasing the grain boundary length. The long length of the B2 grain boundary due to the small B2 grain size appeared to assist the hydrogenation of the alloy by acting as pathways for supplying hydrogen to the inside of the alloy.

1. Introduction

Irregular climate patterns and global warming have emerged as crucial challenges in modern society, alongside issues such as the depletion of fossil fuels and environmental pollution. Therefore, developing environmentally friendly renewable sources, such as solar, wind, and hydroelectric power, is essential to prepare various sustainable energy solutions [1]. However, the intermittent supply fluctuation due to seasons or weather conditions makes renewable energy sources need energy storage solutions in the medium or long term. Among different options, making hydrogen using renewable energy and storing it as metal hydrides is a safe and promising midterm energy storage solution.

Hydrogen storage alloys comprise various alloy systems, such as AB, AB₂, and AB₅. TiFe alloys belong to the AB system, which comprises inexpensive elements and has an excellent storage capacity of 1.8 wt%

H₂ at room temperature [2]. Furthermore, TiFe alloys demonstrate a high energy density of (2.3 MJ kg⁻¹) and a remarkable volumetric storage density of (105 kg H₂ m⁻³), making them an ideal candidate for efficient and compact hydrogen storage alloy solutions [3]. Moreover, the hydrogenation and dehydrogenation reactions are reversible and demonstrate stable performance over thousands of cycles [4], making them reliable for various industrial [5,6] and military [7,8] applications. However, the stoichiometric TiFe binary alloy does not react with hydrogen without the cyclic harsh activation treatments of up to 400 °C and 65 atm H₂ [2]. Primarily because exposure to the atmosphere forms a surface oxide layer that inhibits hydrogen activation [9]. In order to easily accomplish the first activation of TiFe alloys, previous researchers attempted diverse treatments, including ball milling [10] surface modification [11], and cold rolling [12]. Among these previous research studies, the element substitution of TiFe alloy to form a secondary phase

* Corresponding author.

** Corresponding author.

*** Corresponding author.

E-mail addresses: ssohn@korea.ac.kr (S.S. Sohn), mse03@kitech.re.kr (H.-K. Park), tjha@kitech.re.kr (T. Ha).

in the matrix was found to be an effective method for obtaining its hydrogen storage property [13–23]. It has been generally considered that the secondary phase works as a hydrogen gateway during the first activation process in mild conditions [24,25].

In particular, various research added different elements, such as Zr, Mn, Cr, La, Ce, V, and LaNi₅, in TiFe alloy by forming a secondary phase in the TiFe alloy to achieve the first hydrogenation in mild conditions [26–31]. Moreover, Dematteis et al. [32] wrote a review paper about various effects of element substitution in TiFe alloys, such as Mn, Be, Zr, Hf, Nb, Mg, and Cr, and reported both enthalpy and entropy values of TiFe alloys based on the absorption and desorption plateau pressure of Pressure-Composition Isotherm (PCI) curves. Among the elements, Mn substitution in TiFe alloys has been considered to improve its H₂ sorption characteristics, and many studies have confirmed that room temperature activation is possible when secondary phases are dispersed in the TiFe matrix [33–36]. Based on the previous research, the hydrogen sorption properties of TiFe_xMn_{1-x} ($x=0\sim0.3$) under various experimental conditions are summarized in Table 1.

Recently, Shim and co-workers [37] conducted high-magnification SEM-EBSD (scanning electron microscope with electron backscatter diffraction detector) analysis of the TiFeZr alloy and TiFeZrCr alloy systems. Particularly, they focused on the small-sized secondary phases (TiFe₂, Ti₂Fe) with higher KAM values, and the smaller secondary phase particle size of the TiFeZr alloy makes the hydrogenation reaction rate of the alloy faster. To the best of the researchers' knowledge, however, the grain size effect of B2 matrix phase on hydrogen absorption kinetics in dual-phase alloys comprised of B2 and C14 Laves has not yet been reported. In this study, by using a Sievert-type volume analyzer and scanning electron microscope-electron backscatter diffraction (SEM-EBSD), the relationship among the grain size, grain boundary length, grain boundary angle of the B2/B2 matrix phase, and the hydrogen absorption kinetics according to the annealing treatment time of the TiFe_{0.8}Mn_{0.2} alloy was compared.

2. Materials and methods

As-cast TiFe_{0.8}Mn_{0.2} ingot was prepared by utilizing vacuum arc melting equipment and using Ti (99.995%), Fe (99.99%), and Mn (99.7%) lumps measuring 10 mm or less as raw materials. After the raw materials were charged on the copper hearth, the hearth-equipped

vacuum chamber was evacuated to about 10⁻⁵ Torr using rotary oil and oil diffusion pumps. Afterward, the chamber was filled with high-purity Ar gas (99.999%). The ingot samples on the water-cooled copper crucible were re-melted five times to achieve a uniform composition.

Then, the ingot was annealed at 1000 °C in a high vacuum (approximately 10⁻⁵ Torr) atmosphere to homogenize the as-cast sample. The annealing condition is as follows: the ingot was heated to 1000 °C, with a heating rate of 10 °C/min, and held for 10 and 20 h. The choice of 1000 °C was based on the need to ensure sufficient elemental diffusion to achieve phase equilibrium within a reasonable timeframe, as lower temperatures would significantly slow the diffusion process and extend the time required for phase stabilization. Thermo-Calc software was employed to predict phase formation behavior at this temperature, further supporting its selection.

The annealing was conducted under vacuum conditions to prevent contamination and oxidation while enabling a controlled cooling process. The slow cooling rate under vacuum facilitates the material's gradual approach toward its equilibrium phase fraction. After the annealing treatment, the ingot was cooled to room temperature under the furnace's cooling condition. The as-cast, 10 h annealed, and 20 h annealed samples are hereinafter referred to as AS, 10HA, and 20HA, respectively.

Then, the as-cast and annealed alloy samples were pulverized and characterized by X-ray Powder Diffraction (XRD) using a PANalytical Empyrean diffractometer with Cu K_α radiation. The phase fraction and lattice parameters of all samples were quantified by Rietveld refinement using the HighScore Plus software (version 4.1). The phase morphology and chemical composition of the samples were characterized through field emission scanning electron microscopy (FE-SEM; QUANTA FEG 250, FEI) using energy-dispersive X-ray spectroscopy (EDS; EDAX, Octane Elite). Meanwhile, the phase crystal structure and orientation were analyzed through SEM-EBSD (EDAX, Velocity Super). Based on the calculation using the Ti/TiAl-based alloy database (version 8.5.1.0017) of the Thermo-Calc software, the temperature-dependent equilibrium phase fractions and the equilibrium chemical composition of each phase at 1000 °C were determined.

Evaluation of the activated samples' hydrogen absorption kinetics is measured by Sieverts-type volumetric analyzer (MICROTRAC MRB, BELSORP HP) at 20 °C under 40 bar H₂. Before that, the activation process and degassing process are conducted as follows: first of all, the

Table 1
Comparison of the alloy composition, phase number, and main hydrogenation properties of TiFe_{1-x}Mn_x ($x=0\sim0.3$) systems.

| Alloy | Number of Phase | Material Processing | Cycle number for activation | Activation | Temperature [°C] | Pressure [bar] | Hydrogenation kinetics [min] | H ₂ capacity [wt%] | Maximum H ₂ storage [wt%] | Ref. |
|---|-----------------------|-----------------------|-----------------------------|------------|------------------|----------------|------------------------------|-------------------------------|--------------------------------------|------|
| TiFe TiFe _{0.9} Mn _{0.1} | Single phase | Pulverizing | 1 cycle | x | 20 | 40 | - | - | - | [35] |
| | | Pulverizing | 1 cycle | o | 25 | 40 | 6000 | 1.55 | 1.55 | [38] |
| | | Pulverizing | 1 cycle | x | 20 | 40 | - | - | - | [35] |
| | | Pulverizing | 1 cycle | o | 25 | 40 | 6000 | 1.6 | 1.6 | [39] |
| | | Ball milling | 1 cycle | o | 25 | 40 | 1000 | 1.4 | 1.4 | |
| | | Casting | 1 cycle | o | Room Temp. | 39 | 2880 | - | - | [15] |
| | | Annealing | 1 cycle | o | Room Temp. | 39 | 2880 < | - | - | [15] |
| | | Casting | 1 cycle | x | 30 | 21 | - | - | - | [40] |
| TiFe _{0.85} Mn _{0.15} | High pressure torsion | 1 cycle | o | 30 | 21 | 1 | - | 1.3 | 1.6 | [40] |
| | | Casting | 1 cycle | o | Room Temp. | 39 | 1440 | - | - | [15] |
| | | Annealing | 1 cycle | o | Room Temp. | 39 | 1440 < | - | - | [15] |
| | | Pulverizing | 1 cycle | o | 20 | 40 | 120 | 0.18 | - | [35] |
| | | Casting | 1 cycle | o | 20 | 40 | 1200 | 1.28 | - | [3] |
| | | Pulverizing | 3 cycles | o | 30 | 40 | 60 | 1.7 | 1.7 | [3] |
| | | Pulverizing | 3 cycles | o | 50 | 40 | 60 | 1.6 | 1.6 | [3] |
| | | Pulverizing | 3 cycles | o | 70 | 40 | 60 | 1.5 | 1.5 | [3] |
| TiFe _{0.7} Mn _{0.3} | Dual phase | Casting | 3 cycles | o | 20 | 40 | 50 | 1.6 | 1.6 | [36] |
| | | Atomization | 3 cycles | o | 20 | 40 | 20 | 1.6 | 1.6 | [36] |
| | | Pulverizing | 1 cycle | o | 20 | 40 | 120 | 1.59 | - | [35] |
| | | Casting | 1 cycle | o | 20 | 21 | 700 | 1.4 | - | [40] |
| | | High pressure torsion | 1 cycle | o | 30 | 21 | 1 | 1.3 | - | [40] |

ingot was pulverized and sieved to adjust the powder size in the range of 100–150 μm to eliminate the particle size effect on the activated hydrogenation kinetics. Secondly, the pulverized powder was exposed to air for 1 h to induce surface oxidation, reflecting industrial application conditions. Thirdly, ~0.5 g of powder each is repeatedly exposed to 40 bar H₂ at 20 °C for ensuring the all samples are fully activated. After then, hydrogen degassing of the alloy samples is conducted under the dynamic vacuum (2.7×10^{-3} Torr) and 100 °C for 2 h. This process was repeated five times until the pressure drop stabilized, ensuring uniform activation. The above experimental conditions were chosen to replicate the industrialized hydrogen storage conditions and ensure reproducibility in assessing hydrogen absorption performance.

3. Results

Fig. 1(a) represents the XRD patterns of the AS, 10HA, and 20HA samples. According to the Ti–Fe binary phase diagram, the TiFe phase shows the BCC B2 structure, and the Fe₂Ti phase presents the C14 Laves structure [41]. In the Ti–Fe–M ternary alloy system, the C14 Laves phase coexists with the B2 phase by substituting Fe with both Mn and Cr or either of these two [26,28]. The three samples in this study have two phases, which are B2 and C14 Laves. In the XRD patterns, the peak

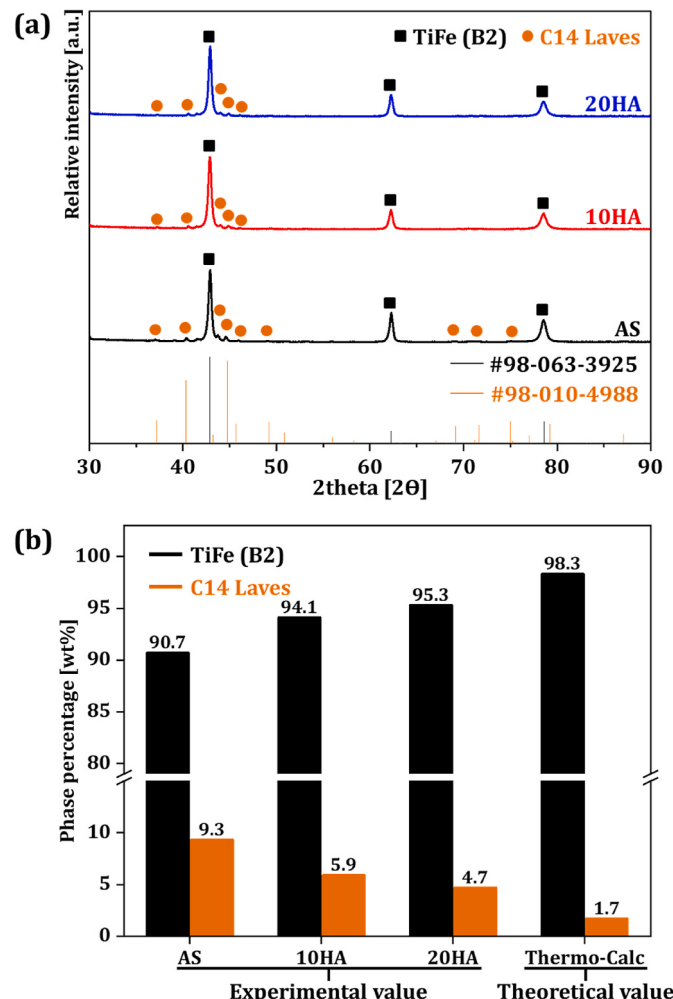


Fig. 1. X-ray Powder Diffraction (XRD) patterns (a) of the as-cast, 10h annealed, and 20h annealed (AS, 10HA, and 20HA) samples, showing the relative intensity of B2 (ICSD #98-063-3925) and C14 Laves (ICSD #98-010-4988) phases; (b) phase fractions of B2 and C14 Laves phases in the samples, compared with the equilibrium phase fraction predicted at 1000 °C based on Thermo-Calc software calculations.

intensity of the C14 Laves phase decreased during the annealing treatment.

Using the XRD patterns of three samples, the phase fraction and lattice parameters were quantified using the Rietveld refinement method. **Fig. 1(b)** shows the phase percentage (wt%) of the samples. The B2 phase percentage in the AS, 10HA, and 20HA samples were 90.4, 94.6, and 95.1 wt%, respectively, showing a positive correlation between the B2 phase percentage and the annealing time. On the other hand, the C14 Laves phase percentage in the AS sample was 9.6 wt%, further decreasing to 5.4 wt% and 4.9 wt% after the application of the annealing treatment for 10 h and 20 h, respectively.

The lattice parameters of the B2 and C14 Laves phases are represented in **Table 2**. For the AS, 10HA, and 20HA samples, the lattice parameters of the B2 phase were 2.979, 2.980, and 2.981 Å. In the AS sample, the lattice parameter of the C14 Laves phase was $a = 4.833$ Å and $c = 7.938$ Å. After the annealing treatment, the values changed to $a = 4.820$ Å and $c = 7.910$ Å for the 10HA sample, and $a = 4.817$ Å and $c = 7.884$ Å for 20HA. As the annealing time increased, the lattice parameter of the B2 phase also changed slightly. However, the lattice parameters of the C14 Laves phase changed more drastically than that of the B2 phase.

Fig. 2 shows the microstructures of the AS, 10HA, and 20HA samples using the secondary electron (SE) mode at low magnification and backscattered electron (BSE) mode at high magnification. From the low magnification micrograph of the AS sample, it was found that the sample mainly comprised the bright phase and the dark precipitated phase dispersed in the bright phase grains. The drastic decrement of the dark precipitates was observed after the 10 h annealing treatment, and the fragmented shape of the second-phase regions might be attributed to the partial transformation of C14 Laves into B2 during the annealing. After the 20 h annealing treatment, the area fraction of the secondary phase decreased, and its color became noticeably brighter than the matrix phase following changes in the chemical composition of each phase.

Furthermore, **Fig. 3** shows that the chemical composition of the dark and bright areas in the AS sample is $\text{Ti}_{50.3}\text{Fe}_{41.8}\text{Mn}_{7.9}$ and $\text{Ti}_{39.7}\text{Fe}_{43}\text{Mn}_{17.3}$, respectively. From the C14 Laves phase, the Ti content decreased, and the Mn content increased as the annealing time was prolonged. In contrast, the B2 phase shows almost the same elemental composition even after the 20 h annealing treatment. After the sample is annealed for 20 h, the composition of the dark and bright areas changed to $\text{Ti}_{50}\text{Fe}_{41.4}\text{Mn}_{8.6}$ and $\text{Ti}_{37.2}\text{Fe}_{39.9}\text{Mn}_{22.9}$, respectively. When considering the calculated composition at 1000 °C using Thermo-Calc software, it can be assumed that the dark area is the B2 phase, and the bright area is the C14 Laves phase.

The equilibrium phase percentage of the $\text{TiFe}_{0.8}\text{Mn}_{0.2}$ alloy calculated by the Thermo-Calc software is presented in **Fig. 4**. The equilibrium percentage of the B2 phase and the C14 Laves phase at 1000 °C is 98.3 wt% and 1.7 wt%, respectively. The percentage of the B2 phase increased as the temperature rose, reaching a maximum of 98.38 wt% at 960 °C. Afterward, the B2 phase fraction slightly decreased in the range of 960 °C–1130 °C. On the other hand, the percentage of the C14 Laves phase decreased as the temperature increased, reaching a minimum of 1.62 wt% at 960 °C. Meanwhile, the C14 Laves phase fraction slightly increased at around 960 °C–1130 °C, reaching a maximum of 20.06 wt% at 1247 °C. The liquid phase started to form at 1130 °C, and the alloy comprised of the B2, C14 Laves, and liquid phases finally turned into the liquid single phase at 1291 °C.

Fig. 5 shows the activated hydrogenation kinetics of the AS, 10HA, and 20HA samples. As mentioned above, all alloys were fully hydrogenated five times and degassed for 2 h at 100 °C before comparing the hydrogen absorption kinetics. All three samples were found to have similar storage capacities of about 1.81 wt% H₂. When considering the storage time, which reached 1.6 wt% H₂, the AS sample took 1.97 min, the 10HA sample required 5.92 min, and the 20HA sample needed 11.3 min at 88% of the maximum H₂ capacity. The more homogenization annealing-treated sample showed more sluggish absorption kinetics,

Table 2

Calculated lattice parameters and cell volume after homogenization annealing for the B2 phase and C14 Laves phase analyzed using the XRD Rietveld method together with crystallographic properties of TiFe, TiMn₂ phases based on the ICSD database [42,43].

| Sample | B2 phase | | C14 Laves phase | | |
|--|---------------------------|-------------------------------|---------------------------|---------------------------|-------------------------------|
| | Lattice parameter a [Å] | Cell volume [Å ³] | Lattice parameter a [Å] | Lattice parameter c [Å] | Cell volume [Å ³] |
| AS | 2.979 | 26.43(7) | 4.833 | 7.938 | 160.57(4) |
| 10HA | 2.980 | 26.46(4) | 4.820 | 7.910 | 159.14(8) |
| 20HA | 2.981 | 26.49(0) | 4.817 | 7.884 | 158.42(7) |
| TiFe [42] (ICSD #98-063-3925) | 2.9790 | 26.44 | — | — | — |
| TiMn ₂ [43] (ICSD #98-010-4988) | — | — | 4.8330 | 7.9380 | 160.57 |

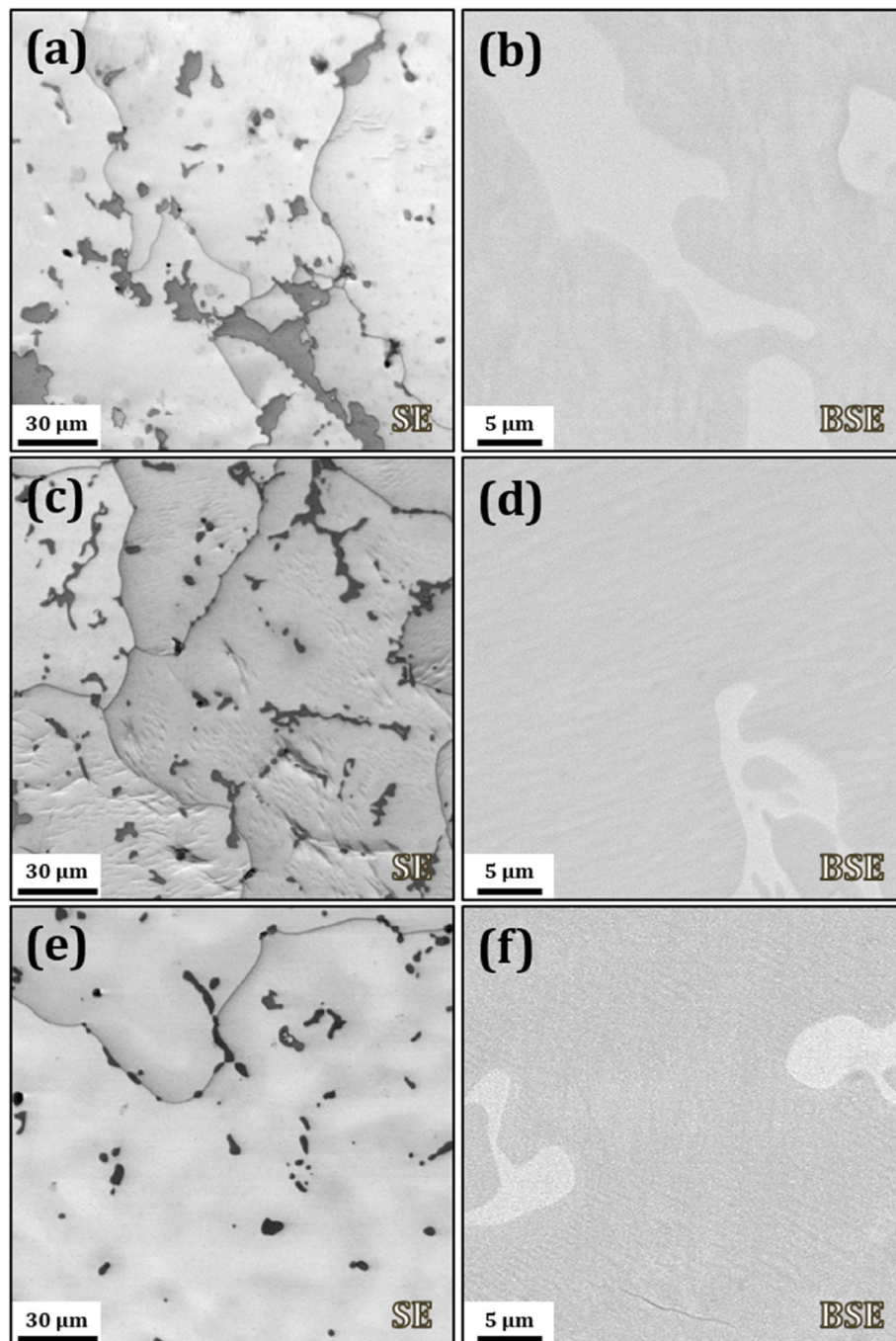


Fig. 2. Secondary electron (SE) micrographs of the (a) as-cast (AS), (c) 10 h annealed (10HA), and (e) 20 h annealed (20HA) samples at low magnification. Backscattered electron (BSE) micrographs of the (b) AS, (d) 10HA, and (f) 20HA samples at high magnification.

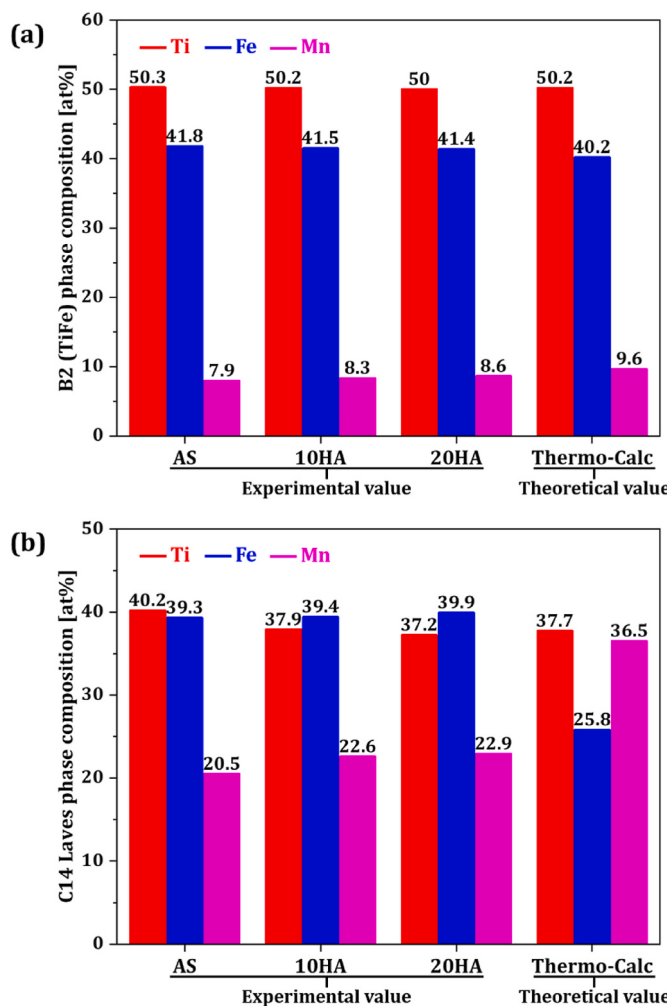


Fig. 3. Chemical composition of the (a) B2 and (b) C14 Laves phases in the as-cast, 10 h annealed, and 20 h annealed (AS, 10HA, and 20HA) samples, respectively. The calculated equilibrium chemical composition of each phase at 1000 °C is plotted together using Thermo-Calc software, respectively.

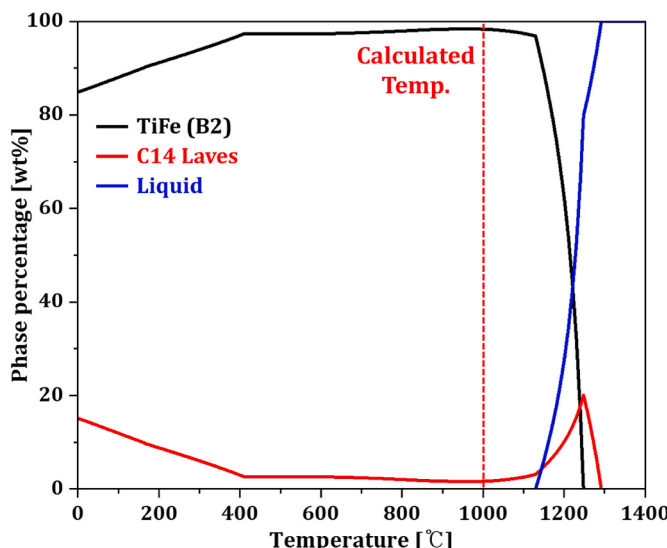


Fig. 4. Phase formation behavior of TiFe_{0.8}Mn_{0.2} alloy calculated using the Thermo-Calc software.

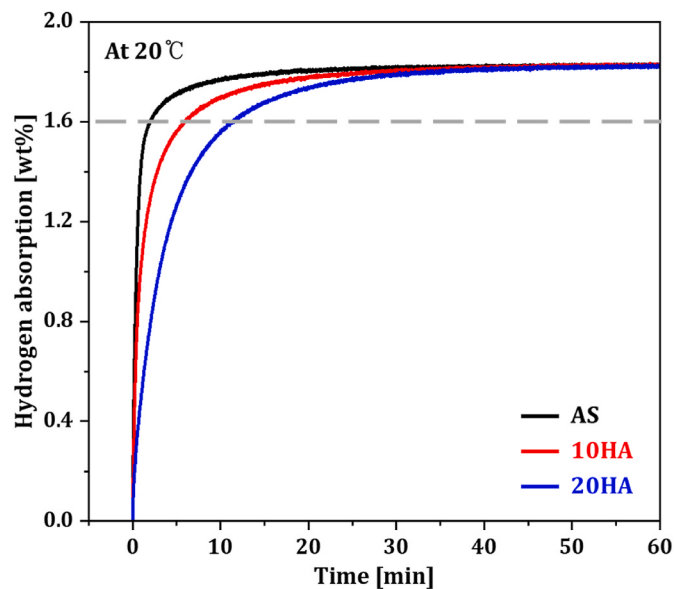


Fig. 5. Activated hydrogenation kinetics profile of the as-cast, 10 h annealed, and 20 h annealed (AS, 10HA, and 20HA) samples.

but all samples were almost hydrogenated after 46 min. It is worth noting that the hydrogen absorption kinetics curve of 10HA is in the middle of the absorption curves of the AS and 20HA samples.

Fig. 6 presents the grain boundary and size changes of TiFe_{0.8}Mn_{0.2} alloys following homogenization annealing treatment based on the SEM-EBSD results. It was observed that the total length of grain boundaries in the B2 phase decreased as the average grain size of the B2 phase increased during homogenization annealing. After the 10 h annealing treatment, the total length of the boundary decreased from 70.4 mm to 34.3 mm, while the average grain size of the sample increased from 175 μm to 215 μm. For the AS sample, almost all the rotation angle boundaries between the dispersed C14 Laves phase precipitates and the B2 matrix phase was more than 15°. However, several rotation angle boundaries between the dispersed C14 Laves phase precipitates and the B2 matrix phase at the 20 h annealed sample were changed to range from 5° to 15°. Considering the IPF color code on the B2 phase, the B2/B2 boundaries marked in green were similarly oriented but with clearly distinct grains. However, the B2/B2 boundaries colored in red showed almost the same orientation, so it was presumed to be residual dendrite boundaries that initially formed during the casting of the AS sample.

In Fig. 7, the grain size distribution and standard deviation of the three samples, as well as their calculated average grain sizes, are shown. As the homogenization annealing time increased, the grain size distribution shifted from 175 μm to 215 μm and reached 256 μm. Moreover, as the annealing time increased, the standard deviation of each sample also rose from 9.36 for the AS sample to 15.07 for the 20HA sample. Looking at the 10HA and 20HA samples, the distribution begins to split into two parts, with the first part remaining in the 0–250 μm range and the second part growing above 300 μm. In particular, for the 20HA sample, the grain distribution became quite irregular, and anomalous grains larger than 450 μm were observed. However, the 20 h annealing treatment at 1000 °C was insufficient in removing all small grains ranging from 0 μm to 50 μm.

4. Discussion

The arc melting process is one of the most convenient ways for melting Ti, Fe, and Mn elements to synthesize the TiFe_{0.8}Mn_{0.2} alloy at a temperature higher than 3000 °C. During the cooldown of melts on the water-cooled copper hearth, Fig. 4 shows that the primary C14 Laves phase began to form inside the melt at 1291 °C, and the B2 phase also

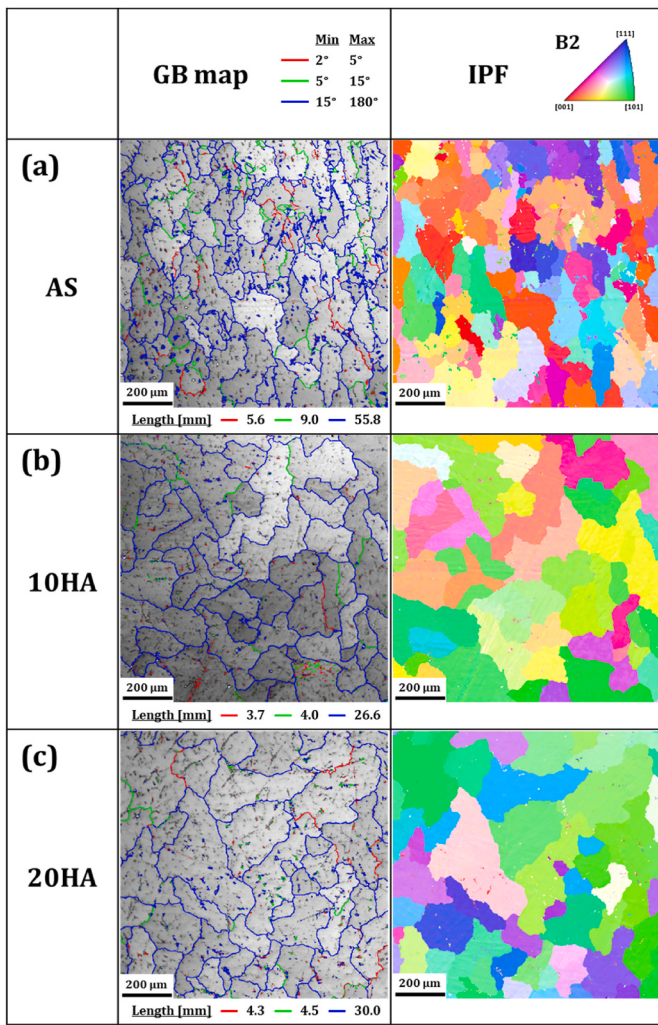


Fig. 6. Scanning Electron Microscope–Electron Backscatter Diffraction (SEM-EBSD) analyzed grain boundary map and inverse pole figure (IPF) maps of the (a) as-cast (AS), (b) 10 h annealed (10HA), and (c) 20 h annealed (20HA) samples.

started to form at 1247 °C from the residual liquid phase. In Fig. 1, a decreasing trend in C14 Laves was clearly observed between the AS and 10HA samples with 10 h annealing, but the additional annealing did not effectively minimize the phase fraction of C14 Laves. Based on these results, the rapid cooling rate in the arc melting process inhibits the formation of equilibrium phase fractions, whereas subsequent annealing promotes the formation of phases closer to the equilibrium phase fractions predicted by thermodynamic calculations in Fig. 4.

The microstructural features of the three samples from Figs. 2–6 showed that the C14 Laves phase is dispersed in the B2 matrix phase. Compared to the large area fraction of the C14 Laves phase in the AS sample, there is a significantly smaller amount of secondary phase residues inside the B2 matrix phase in the 10HA and 20HA samples. Among the chemical compositions of each phase in Fig. 3, the increase in Mn content and decrease in Ti in the C14 Laves phase due to 10 h annealing induced large changes in lattice parameters and unit cell volume, according to Table 2. The predicted equilibrium chemical composition and phase fraction of B2 matrix phase, and C14 Laves phase both approach equilibrium with annealing treatment. However, the evolution to the equilibrium chemical composition and phase fraction of the C14 Laves phase is too slow even after annealing the TiFe_{0.8}Mn_{0.2} alloy at 1000 °C for 20 h.

Compared with previous reports about the lattice parameters of TiFe

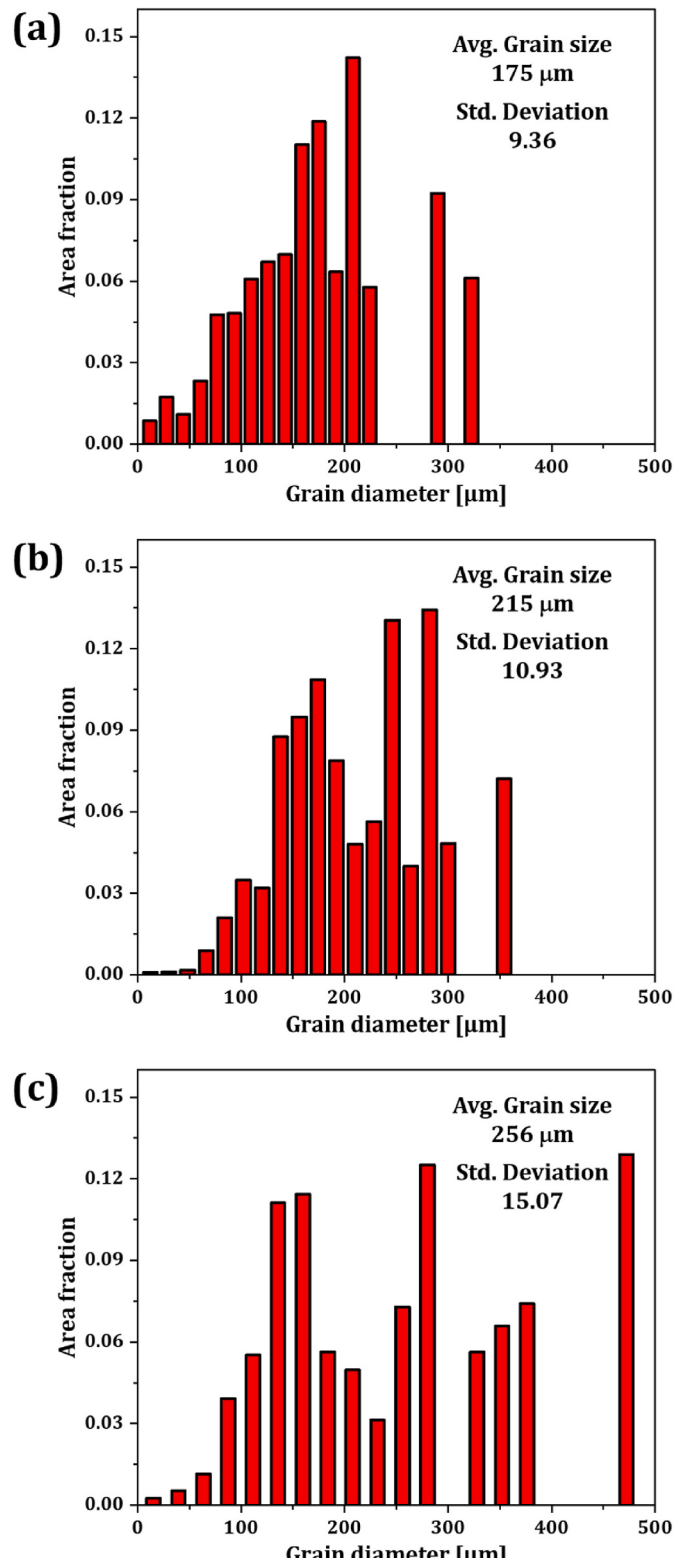


Fig. 7. Grain diameter distribution and its standard deviation results of the (a) as-cast (AS), (b) 10 h annealed (10HA), and (c) 20 h annealed (20HA) samples using Scanning Electron Microscope–Electron Backscatter Diffraction (SEM-EBSD) analysis.

[44] and Fe₂Ti [45] with Table 2, the partial substitution of Mn to Fe in TiFe alloy distinctly increases the lattice parameter of TiFe. Still, the effect of Mn addition is more complex in the Fe₂Ti phase. When comparing the XRD Rietveld analysis results of Fe₂Ti [45] with the C14 Laves phase in AS, 10HA, and 20HA alloys, it was observed that both the a-axis and c-axis increased in the Laves unit cell. This trend was also observed when comparing the lattice constants of TiMn₂ [43] and the lattice constants of Fe₂Ti [45], indicating an increase in the C14 Laves' lattice constants with increasing Mn content. It might be due to the atomic sizes of Ti, Fe, and Mn in the metal bond that comprises the C14 Laves phase were expected to be 147 pm [46], 126 pm, and 127 pm [47], respectively.

The grain boundary maps and its IPF maps in Fig. 6 showed that the annealing treatment minimized the total grain boundary length by decreasing the C14 Laves secondary phase. Considering the constant chemical composition of the B2 matrix in Fig. 3(a), it appeared that a part of the C14 Laves phase excessively formed in the AS sample was converted into the B2 matrix phase. As shown in Fig. 2(e), the dispersed spherical secondary phases were generally located in a dark pattern at the B2 matrix phase of the 20HA sample. Considering the element composition results in Fig. 3, this pattern was likely due to the slight chemical composition fluctuation during the 20 h heat treatment at 1000 °C.

Fig. 5 shows the hydrogen absorption kinetics of the AS, 10 HA, and 20 HA powder samples with particle sizes ranging from 100 μm to 150 μm. Considering that the Rietveld phase fraction of the C14 Laves phase decreased from 9.3 wt% for the AS sample to 4.7 wt% for the 20HA sample, the B2 matrix almost solely attributed the hydrogen absorption kinetics to the 20HA sample. According to the hydrogen storage results of the 20HA sample with an increased B2 phase fraction, the residual C14 Laves phase was expected to have similar hydrogen storage properties as the B2 phase.

Considering the present results based on the fact that the Mn content of B2 phase increases with increasing annealing time, and that both the phase fraction and the average grain size of B2 phase also increase, it is necessary to review the interesting results previously reported by Edalati et al. [40] and Lee et al. [36]. Edalati investigated the co-effect of Mn addition, and high-pressure torsion (HPT) treatment on the hydrogen sorption properties of TiFe alloy. Based on the calculated hydride formation energy values according to the element content using the density functional theory (DFT), he suggested that the hydride phase was more likely to form when Mn was substituted at the Fe site of the Ti–Fe–Mn ternary system. He also suggested that defects formed by HPT lower both the activation temperature required for hydrogenation and the effective temperature required for the phase transformation of hydrides. By using the atomized powder method to fabricate TiFe_{0.8}Mn_{0.2} alloy, Lee compared the activated hydrogen absorption kinetics with that of crushed ingot [36]. The atomized powder exhibits faster hydrogen absorption kinetics than the crushed ingot, which was proposed to be due to the fine microstructure in the powder.

Therefore, the three major parameters affecting the hydrogenation kinetics of TiFe_{1-x}Mn_x ($x = 0.15\text{--}0.3$) alloy are defects, Mn content, and microstructure. For example, the measured activated hydrogenation rate of the 20HA alloy is slow even when the Mn content of B2 phase increases, because the internal defects are reduced, and its microstructure is coarsened during the annealing process. Especially, the analyzed average grain sizes of the AS, 10HA, and 20HA samples in Fig. 7 were 175 μm, 215 μm, and 256 μm, respectively. The hydrogen absorption kinetics of all samples were measured as pulverized state using the powder falling in the range of 100 μm–150 μm. Although the Mn content of the B2 phase was increased following the heat treatment, the deterioration of the hydride formation kinetics due to the decrease in the total grain boundary length cannot be overcome. Based on that, each particle in the AS sample was more likely to have at least one B2/B2 grain boundary, and each particle in the 20HA sample was more likely not to have a B2/B2 grain boundary. Thus, the defects, which appeared

as a long grain boundary in the as-cast TiFe_{0.8}Mn_{0.2} alloy, worked as hydrogen channels, accelerating the hydrogen diffusion into the alloy and promoting hydride formation.

5. Conclusions

In this study, the microstructural features of the as-cast and annealed TiFe_{0.8}Mn_{0.2} alloys were investigated using SEM-EDS-EBSD analysis, along with their hydrogen absorption properties. Unlike previous studies that mainly focused on analyzing hydrogen storage characteristics by changing mechanical treatment process or substituting other elements, this study introduced annealing treatment to change the phase fraction, grain size, and chemical composition of the alloy. These changes were compared with the equilibrium phase predicted by Thermo-Calc software, and microstructural features obtained from the SEM-EBSD. The hydrogen absorption kinetics of AS, 10HA, and 20HA were analyzed and interpreted based on the co-effect of defects, Mn content, and microstructure in the samples.

- BCC (B2) structured TiFe phase and C14 Laves structured Fe₂Ti phase are observed in the as-cast and two annealed samples. Phase fraction of the C14 Laves phase was significantly reduced after 10 h annealing, which consistent with the Rietveld refinement results of X-ray diffraction patterns of three samples.
- The SEM - SE micrographs of the annealed samples indicated that the second-phase C14 Laves exhibited a dispersed shape, which was presumably caused by the partial transformation of Fe₂Ti into TiFe during the annealing.
- Previously activated three samples are all immediately hydrogenated without the incubation period when 40 bar H₂ is applied at 20 °C. As the annealing treatment period of the alloy increased, slower hydrogen absorption kinetics were observed. After 46 min of hydrogenation, all the samples are fully hydrogenated, exhibiting 1.81 wt% H₂ with a similar storage capacity.
- The hydrogenation kinetics of the alloy at room temperature were strongly influenced by the grain size of the B2 matrix phase. The as-cast sample, which contained a smaller average grain size of the matrix phase, was hydrogenated more quickly than the 10 h and 20 h annealed samples, which contained larger average grain sizes.

Grain boundaries, which appear as defects in the as-cast TiFe_{0.8}Mn_{0.2} alloy powder, were shown to function as hydrogen pathways, accelerating hydrogen diffusion and facilitating hydride formation. However, previous studies have reported that Mn substitution at the Fe site decreases the hydride formation energy, which does not fully explain the observed reduction in hydrogen absorption kinetics despite the increased Mn content after annealing. This study highlights that the coarsening of grains after annealing, as revealed by EBSD analysis, reduces the overall grain boundary length available for hydrogen diffusion, thereby contributing to the decrease in hydrogen absorption kinetics.

In prior studies, the correlation between grain boundary angles and hydrogen absorption kinetics has not been reported. Based on the results of this study, where the length of high-angle grain boundaries decreased significantly more than that of low-angle grain boundaries after annealing treatment, it is inferred that high-angle grain boundaries have a greater influence on hydrogen absorption kinetics. To investigate this phenomenon, it is necessary to study the effects of various intentionally induced mechanical defects on the hydrogen sorption properties of the alloy. For this purpose, mechanical processes such as high pressure torsion (HPT), ball milling, high energy milling, hot rolling and cold rolling can be utilized to obtain finer grain structures in the samples. The grain size and the amount of dislocations in the alloys can be analyzed using TEM, revealing the relationship between defect type and hydrogen sorption kinetics.

Declaration of competing interest statement

The authors declare that they have no known competing financial interests or personal relationships that could have appeared to influence the work reported in this paper.

Acknowledgments

This work was supported by the Korea Institute of Industrial Technology (KITECH EH-24-0007); the National Research Foundation of Korea (NRF), funded by the Ministry of Science and ICT [grant no. 2019M3E6A1103910]; the Ministry of Trade, Industry and Energy through the machinery and equipment industry technology development project [grant no. 20018661]; and the National Research Council of Science & Technology (NST) grant by the Korea government (MSIT) (No. GTL24051-300).

References

- [1] Christopher K, Dimitrios R. A review on exergy comparison of hydrogen production methods from renewable energy sources. *Energy Environ Sci* 2012;5:6640–51. <https://doi.org/10.1039/c2ee01098d>.
- [2] Reilly J, Wiswall R. Formation and properties of iron titanium hydride. *Inorg Chem* 1974;13:218–22. <https://doi.org/10.1021/ic50131a043>.
- [3] Park KB, Kwak R-H, Ko W-S, Sohn SS, Park H-K, Fadonougo JO. Exploring the kinetics and thermodynamics of $TiFe_{0.8}Cr_xMn_{0.2-x}$ hydrogen storage alloys. *Int J Hydrogen Energy* 2024;93:832–44. <https://doi.org/10.1016/j.ijhydene.2024.10.432>.
- [4] Liu H, Zhang J, Sun P, Zhou C, Liu Y, Fang ZZ. An overview of TiFe alloys for hydrogen storage: structure, processes, properties, and applications. *J Energy Storage* 2023;68:10772. <https://doi.org/10.1016/j.est.2023.10772>.
- [5] Endo N, Suzuki S, Goshima K, Maeda T. Operation of a bench-scale TiFe-based alloy tank under mild conditions for low-cost stationary hydrogen storage. *Int J Hydrogen Energy* 2017;42:5246–51. <https://doi.org/10.1016/j.ijhydene.2016.11.088>.
- [6] Endo N, Shimoda E, Goshima K, Yamane T, Nozu T, Maeda T. Operation of a stationary hydrogen energy system using TiFe-based alloy tanks under various weather conditions. *Int J Hydrogen Energy* 2020;45:207–15. <https://doi.org/10.1016/j.ijhydene.2019.10.240>.
- [7] Psoma A, Sattler G. Fuel cell systems for submarines: from the first idea to serial production. *J Power Sources* 2002;106:381–3. [https://doi.org/10.1016/S0378-7753\(01\)01044-8](https://doi.org/10.1016/S0378-7753(01)01044-8).
- [8] Von Colbe JB, Ares J-R, Barale J, Baricco M, Buckley C, Capurso G, et al. Application of hydrides in hydrogen storage and compression: achievements, outlook and perspectives. *Int J Hydrogen Energy* 2019;44:7780–808. <https://doi.org/10.1016/j.ijhydene.2019.01.104>.
- [9] Lv P, Liu Z. Effect of high zirconium content on hydrogenation properties and anti-poisoning ability of air-exposed TiFe alloy. *J Mater Res Technol-JMRT* 2019;8: 5972–83. <https://doi.org/10.1016/j.jmrt.2019.09.072>.
- [10] Emami H, Edalati K, Matsuda J, Akiba E, Horita Z. Hydrogen storage performance of TiFe after processing by ball milling. *Acta Mater* 2015;88:190–5. <https://doi.org/10.1016/j.actamat.2014.12.052>.
- [11] Williams M, Lototsky M, Davids M, Linkov V, Yartys V, Solberg J. Chemical surface modification for the improvement of the hydrogenation kinetics and poisoning resistance of TiFe. *J Alloys Compd* 2011;509:S770–4. <https://doi.org/10.1016/j.jallcom.2010.11.063>.
- [12] Vega L, Leiva D, Neto RL, Silva W, Silva R, Ishikawa T, et al. Mechanical activation of TiFe for hydrogen storage by cold rolling under inert atmosphere. *Int J Hydrogen Energy* 2018;43:2913–8. <https://doi.org/10.1016/j.ijhydene.2017.12.054>.
- [13] Jang T, Han J, Jai-Young L. Effect of substitution of titanium by zirconium in TiFe on hydrogenation properties. *J Less-Common Met* 1986;119:237–46. [https://doi.org/10.1016/0022-5088\(86\)90684-3](https://doi.org/10.1016/0022-5088(86)90684-3).
- [14] Lee S-M, Perng T-P, Juang H-K, Chen S-Y, Chen W-Y, Hsu S-E. Microstructures and hydrogenation properties of $TiFe_{1-x}M_x$ alloys. *J Alloys Compd* 1992;187:49–57. [https://doi.org/10.1016/0925-8388\(92\)90519-F](https://doi.org/10.1016/0925-8388(92)90519-F).
- [15] Lee S-M, Perng T-P. Effect of the second phase on the initiation of hydrogenation of $TiFe_{1-x}M_x$ ($M = Cr, Mn$) alloys. *Int J Hydrogen Energy* 1994;19:259–63. [https://doi.org/10.1016/0360-3199\(94\)90095-7](https://doi.org/10.1016/0360-3199(94)90095-7).
- [16] Kamegawa A, Kudo H, Takamura H, Okada M. Protium absorption and desorption properties of bcc Ti-Fe solid solution alloys stabilized by Mo addition. *Mater Trans* 2003;44:991–4. <https://doi.org/10.2320/matertrans.44.991>.
- [17] Wang X, Chen R, Chen C, Wang Q. Hydrogen storage properties of Ti_xFe_{1-x} y wt.% La and its use in metal hydride hydrogen compressor. *J Alloys Compd* 2006;425: 291–5. <https://doi.org/10.1016/j.jallcom.2006.01.025>.
- [18] Guéguen A, Latroche M. Influence of the addition of vanadium on the hydrogenation properties of the compounds $TiFe_{0.9}V_x$ and $TiFe_{0.8}Mn_{0.1}V_x$ ($x = 0, 0.05$ and 0.1). *J Alloys Compd* 2011;509:5562–6. <https://doi.org/10.1016/j.jallcom.2011.02.036>.
- [19] Jain P, Gosselin C, Huot J. Effect of Zr, Ni and Zr_7Ni_{10} alloy on hydrogen storage characteristics of TiFe alloy. *Int J Hydrogen Energy* 2015;40:16921–7. <https://doi.org/10.1016/j.ijhydene.2015.06.007>.
- [20] Leng H, Yu Z, Yin J, Li Q, Wu Z, Chou K-C. Effects of Ce on the hydrogen storage properties of $TiFe_{0.9}Mn_{0.1}$ alloy. *Int J Hydrogen Energy* 2017;42:23731–6. <https://doi.org/10.1016/j.ijhydene.2017.01.194>.
- [21] Razafindramanana V, Gorse S, Huot J, Bobet JL. Effect of hafnium addition on the hydrogenation process of TiFe alloy. *Energies* 2019;12:3477. <https://doi.org/10.3390/en12183477>.
- [22] Gosselin C, Huot J. First hydrogenation enhancement in TiFe alloys for hydrogen storage doped with yttrium. *Metals* 2019;9:242. <https://doi.org/10.3390/met9020242>.
- [23] Patel AK, Duguay A, Tougas B, Schade C, Sharma P, Huot J. Microstructure and first hydrogenation properties of TiFe alloy with Zr and Mn as additives. *Int J Hydrogen Energy* 2020;45:787–97. <https://doi.org/10.1016/j.ijhydene.2019.10.239>.
- [24] Patel AK, Duguay A, Tougas B, Neumann B, Schade C, Sharma P, et al. Study of the microstructural and first hydrogenation properties of TiFe alloy with Zr, Mn and V as additives. *Processes* 2021;9:1217. <https://doi.org/10.3390/pr9071217>.
- [25] Alam MM, Sharma P, Huot J. Effect of addition of rare earth element La on the hydrogen storage properties of TiFe alloy synthesized by mechanical alloying. *Int J Hydrogen Energy* 2024;50:261–71. <https://doi.org/10.1016/j.ijhydene.2023.07.049>.
- [26] Lv P, Huot J. Hydrogenation improvement of TiFe by adding $ZrMn_2$. *Energy* 2017; 138:375–82. <https://doi.org/10.1016/j.energy.2017.07.072>.
- [27] Romero G, Lv P, Huot J. Effect of ball milling on the first hydrogenation of TiFe alloy doped with 4 wt% $(Zr + 2Mn)$ additive. *J Mater Sci* 2018;53:13751–7. <https://doi.org/10.1007/s10853-018-2301-9>.
- [28] Patel AK, Tougas B, Sharma P, Huot J. Effect of cooling rate on the microstructure and hydrogen storage properties of TiFe with 4 wt% Zr as an additive. *J Mater Res Technol-JMRT* 2019;8:5623–30. <https://doi.org/10.1016/j.jmrt.2019.09.030>.
- [29] Lv P, Liu Z, Dixit V. Improved hydrogen storage properties of TiFe alloy by doping $(Zr + 2V)$ additive and using mechanical deformation. *Int J Hydrogen Energy* 2019; 44:27843–52. <https://doi.org/10.1016/j.ijhydene.2019.08.249>.
- [30] Lv P, Liu Z, Patel AK, Zhou X, Huot J. Influence of ball milling, cold rolling and doping $(Zr + 2Cr)$ on microstructure, first hydrogenation properties and anti-poisoning ability of TiFe alloy. *Mater Int* 2021;27:1346–57. <https://doi.org/10.1007/s12540-019-00501-1>.
- [31] Alam MM, Sharma P, Huot J. On the hydrogen storage properties of cast TiFe mechanically milled with an intermetallic $LaNi_5$ and rare-earth elements La and Ce. *Int J Hydrogen Energy* 2024;50:727–37. <https://doi.org/10.1016/j.ijhydene.2023.08.100>.
- [32] Dematteis EM, Berti N, Cuevas F, Latroche M, Baricco M. Substitutional effects in TiFe for hydrogen storage: a comprehensive review. *Mater Adv* 2021;2:2524–60. <https://doi.org/10.1039/D1MA00101A>.
- [33] Dematteis EM, Cuevas F, Latroche M. Hydrogen storage properties of Mn and Cu for Fe substitution in $TiFe_{0.9}$ intermetallic compound. *J Alloys Compd* 2021;851: 156075. <https://doi.org/10.1016/j.jallcom.2020.156075>.
- [34] Park KB, Fadonougo JO, Park C-S, Lee J-H, Na T-W, Kang H-S, et al. Effect of Fe substitution on first hydrogenation kinetics of TiFe-based hydrogen storage alloys after air exposure. *Int J Hydrogen Energy* 2021;46:30780–9. <https://doi.org/10.1016/j.ijhydene.2021.06.188>.
- [35] Park KB, Ko W-S, Fadonougo JO, Na T-W, Im H-T, Park J-Y, et al. Effect of Fe substitution by Mn and Cr on first hydrogenation kinetics of air-exposed TiFe-based hydrogen storage alloy. *Mater Char* 2021;178:111246. <https://doi.org/10.1016/j.matchar.2021.111246>.
- [36] Lee DH, Kwon HG, Park KB, Im H-T, Kwak RH, Sohn SS, et al. Phase formation behavior and hydrogen sorption characteristics of $TiFe_{0.8}Mn_{0.2}$ powders prepared by gas atomization. *Int J Hydrogen Energy* 2023;48:27697–709. <https://doi.org/10.1016/j.ijhydene.2023.03.289>.
- [37] Lee S-I, Ha T, Lee Y-S, Kim D-I, Suh J-Y, Cho YW, et al. EBSD microstructural analysis of AB-type TiFe hydrogen storage alloys. *Mater Char* 2021;178:111276. <https://doi.org/10.1016/j.matchar.2021.111276>.
- [38] Zeaiter A, Nardin P, Yazdi MAP, Billard A. Outstanding shortening of the activation process stage for a TiFe-based hydrogen storage alloy. *Mater Res Bull* 2019;112: 132–41. <https://doi.org/10.1016/j.materresbull.2018.12.015>.
- [39] Zeaiter A, Chapelle D, Cuevas F, Maynadier A, Latroche M. Milling effect on the microstructural and hydrogenation properties of $TiFe_{0.9}Mn_{0.1}$ alloy. *Powder Technol* 2018;339:903–10. <https://doi.org/10.1016/j.powtec.2018.08.085>.
- [40] Edalati K, Matsuo M, Enami H, Itano S, Alhamidi A, Staykov A, et al. Impact of severe plastic deformation on microstructure and hydrogen storage of titanium-iron-manganese intermetallics. *Scr Mater* 2016;124:108–11. <https://doi.org/10.1016/j.scriptamat.2016.07.007>.
- [41] Okamoto H, Massalski T. Binary alloy phase diagrams, vol. 12. Materials Park, OH, USA: ASM International; 1990. p. 3528–31. <https://doi.org/10.31399/asm.hb.v03.a006247>.
- [42] Thompson P, Reilly J, Hastings J. The application of the Rietveld method to a highly strained material with microtwins: $TiFeD_{1.9}$. *J Appl Crystallogr* 1989;22: 256–60. <https://doi.org/10.1107/S002188988801430X>.
- [43] Costa MmrdA MJM. Electron density in the Laves phase $TiMn_2$ thorium-manganese system. *Port Phys* 1986;17:173–80.
- [44] Duwez P, Taylor JL. The structure of intermediate phases in alloys of titanium with iron, cobalt, and nickel. *JOM* 1950;2:1173–6. <https://doi.org/10.1007/BF03399120>.

- [45] Brückner W, Kleinstück K, Schulze G. Atomie arrangement in the homogeneity range of the laves phases ZrFe₂ and TiFe₂. *Phys Status Solidi B-Basic Res* 1967;23: 475–80. <https://doi.org/10.1002/pssb.19670230206>.
- [46] Perevalova OB, Konovalova EV, Koneva NA. Effect of aluminum concentration on the lattice parameters and mean-square displacements of atoms in Cu-Al and Ti–6Al–4V alloys. *Bull Russ Acad Sci: Phys* 2019;83:693–6. <https://doi.org/10.3103/S1062873819060236>.
- [47] Panpan L, Wang A. Composition dependence of structure, physical and mechanical properties of FeCoNi(MnAl)_x high entropy alloys. *Intermetallics* 2017;87:21–6. <https://doi.org/10.1016/j.intermet.2017.04.007>.